ROYAL SOCIETY
OF CHEMISTRY

Check for updates

N and S co-doped graphene enfolded Ni–Co-layered double hydroxides: an excellent electrode material for high-performance energy storage devices†

Firoz Khan [ID] *

The performance of hybrid supercapacitors (HSCs) can be increased *via* the selection of higher capacitive electrode materials. Thus, layered double hydroxides (LDHs) have received extensive consideration in HSCs owing to their good ion-exchange properties, structural flexibility, and large specific surface area. Ni–Co-based LDHs show better specific capacitance, good synergy, and high-rate capability in aqueous electrolytes. However, LDHs suffer from low conductivity, which curbs the charge transfer and mass diffusion throughout the electrochemical process. Thus, the high performance of LDH-based supercapacitors is impeded. Hence, composites of LDH and conducting materials are used. Owing to its extraordinary conducting property, huge surface area, and cost-effectiveness, reduced graphene oxide (rGO) is used as conducting material for LDH-based composite electrodes. Moreover, *via* the incorporation of heteroatoms (N, S, *etc.*) into rGO, its electrochemical properties are further enhanced. Here, a novel composite electrode is prepared by wrapping Ni–Co-LDH with N and S-co-doped rGO (LDH-rGO-NS) *via* a hydrothermal process. The XPS C 1s spectra established the existence of N and S doping in the rGO. The electrochemical performance is enhanced due to an excellent ion/charge transfer rate because of N and S co-doping. The LDH-rGO-NS electrode offers a good charge transfer resistance of 0.24 Ω. The obtained anodic and cathodic *b*-values are 0.73 and 0.72, respectively. An admirable specific capacitance of 1388 F g^{-1} is accomplished at a sweep rate of 100 mV s^{-1}. Furthermore, the obtained retention capacity is ∼71% after 2000 cycles. Moreover, the achieved specific capacitance is 2193 F g^{-1} at the discharge current density of 5 A g^{-1}. The excellent electrochemical properties reveal the LDH-rGO-NS composites as encouraging electrode materials for HSCs.

1. Introduction

Storing electrical energy is critical for addressing issues related to environmental protection, renewable energy integration, energy sustainability, energy efficiency, and so on.[1,2] Amongst the available electrical energy storing machinery, supercapacitors (SCs) are appropriate for several important applications where prompt power supply and a long-lasting lifetime are essential. SCs possess high power density along with a prolonged life cycle. They also ensure enhanced safety to modern electronic appliances. However, their energy density is quite low in comparison to batteries/fuel cells due to the inherent problem of the two main classes of supercapacitors *i.e.*, electric double-layer capacitors (EDLCs) and pseudocapacitors (PSCs).

To increase the power density along with the energy density, a hybrid structure has been evolved by combining the EDLC and PSC principles into its architecture. Thus, the obtained devices by combining the properties of EDLCs and PSCs are known as hybrid supercapacitors (HSCs). They retain high energy densities in addition to high power densities unlike normal SCs.[3–7] In the present scenario of high-tech electronics and electricity demand, HSCs have arisen as prominent energy storage devices (ESDs) to fulfill the demand of energy scarceness, safety, and security. Owing to their huge potential in electricity storage, portable electronics, and hybrid vehicles, this technology has received substantial consideration by researchers to improve their performance. Moreover, owing to their great performance, prolonged life cycle, tremendous cyclic stability, and ecological friendliness, HSCs are considered promising ESDs. Among the different components of HSCs, the electrode materials directly affect electrochemical performance. The nature and performance of the electrode materials are the basic keys to develop high-performance HSCs with an elongated life cycle along with high energy/power densities.[3,4,6–9] In conventional HSCs,

Interdisciplinary Research Center for Renewable Energy and Power Systems (IRC-REPS), Research Institute, King Fahd University of Petroleum & Minerals (KFUPM), Dhahran-31261, Saudi Arabia. E-mail: firoz.khan@kfupm.edu.sa; Fax: +966 13 8607312; Tel: +966 13 8607019

carbon-based materials are used as a negative electrode (anode during discharge process), while metal compounds (oxides, hydroxides, layered double hydroxide (LDH), metal–metal oxides (MMO)) are used as the positive electrode (cathode during discharge process).[3–8,10] In the past few years, LDHs have received extensive consideration as the anode materials in HSCs owing to their good ion-exchange property, structural flexibility, and huge surface area. The manifold oxidation state LDH is the additional advantage to enhance the performance HSCs. Among the LDHs, Ni–Co-based LDHs (Ni–Co-LDH) showed superior specific capacitance, good synergy, and high-rate capability. Moreover, the microstructure of these materials can be controlled during the synthesis process, which provides greater flexibility to tune the size and structure of LDHs. Another important factor that is essential to control the structural and morphological properties accompanied by crystallinity and capacity of these bi-metallic LDHs is the atomic ratio of the metallic elements. Several researchers studied the influence of the Ni and Co fraction in Ni–Co-LDH. Sun *et al.*[11] reported having nanosheets (1 : 1), nanoplates (1 : 2), and nanorods (1 : 4) of Ni–Co-LDHs through the variation of Ni and Co composition. Yang *et al.*[12] have investigated the dependency of the LDH microstructure on Ni/Co ratio. They have found that nanowire-shaped Ni–Co-LDH was obtained at a 1 : 1 Ni : Co ratio, which disappeared with the reduction of Co content. In another report, Wu *et al.*[6] have prepared Ni–Co-LDHs and nitrogen-doped CNT composite electrodes on Ni foam using different Ni and Co compositional ratios. They have obtained the best capacitance value of 2170 F g^{-1} for Ni and Co atomic ratio of 1 : 1 at 1 A g^{-1}. However, the best cycle constancy was achieved for the Ni and Co atomic ratio of 67 : 33 (approximately 2 : 1). Moreover, like all other LDH materials, Ni–Co-based LDH also endures from low conductivity, thus the charge transfer, as well as mass diffusion, is hampered during the charge/discharge cycling. Thus, the LDH-based HSCs offer a low value of capacitance. Furthermore, the agglomeration in the LDH nanostructures has also been observed, which obstructs the energy density and degrades the cycling constancy of the HSCs. Thus, a composite of conducting material (carbon nanotubes, carbon nanofiber, conducting carbon, graphene, *etc.*) and LDH is used or LDH is directly deposited on nickel foam to overcome this particular issue.[3–6] This approach was found to be effective to enhance the electronic conductivity, which consequences in a better rate of competence, and improved cycling constancy of Ni–Co-LDH. Among all these conductive substrates used to overcome the low conductivity issues of the LDHs, graphene-based composites showed superior performances.[13–16] It is due to graphene's outstanding electrical and thermal conductivity, high mechanical strength, and high specific surface area. Several research groups observed that the graphene's properties can be further twined to enhance its performance, simply by doping and/or co-doping with some heteroatoms, for example, N, S, P, or B. In particular, the co-doping of graphene is getting attention because it can create a unique and synergistically coupled electronic structure.[7,13–17] To reduce the energy-storing cost and minimize the size of the HSCs, the electrochemical performance of the anode materials further needs to be improved.

2. Objectives

The objective of the work is to develop an advanced electrode material for a high-performance electrochemical energy storage device. It is observed that Ni–Co-based LDH offers superior specific capacitance, excellent interaction, and high cycling performance. Due to the low conductivity of Ni–Co-LDH, the electrochemical performance of Ni–Co-LDH based electrodes is hampered. Thus, it creates an obstacle to achieving the high performance of the LDH-based supercapacitors. Hence, the composites of LDH and conducting materials are used. In this regard, herein graphene and Ni–Co-LDH composite was used as a potential electrode material. Furthermore, the advantage of double heteroatoms (N and S) doping in rGO (rGO-NS) is believed to enhance the charge transportation rate. Therefore, the wrapping of Ni–Co-LDH by rGO-NS (LDH-rGO-NS) was used to enhance the surface conductivity of the Ni–Co-LDH and improve the electrochemical performance of the electrode. The structural, morphological, and elemental properties of the LDH-rGO-NS were studied using a variety of techniques (XRD, FE-SEM, TEM, XPS, Raman, *etc.*). Furthermore, the electrochemical properties of the LDH-rGO-NS were also studied to evaluate the performance of the electrode material.

3. Experimental

3.1. Synthesis of rGO-NS

The GO solution was prepared *via* the dispersion of GO powder in deionized (DI) water. Furthermore, the GO nano-sheets were synthesized by ultra-sonication for 4 h. Then 0.01 mole thiourea was dissolved to the GO solution. The pH value was kept in the range of 8–9. The resultant solution (**solution A**) was stirred for 30 min.

3.2. Synthesis of Ni–Co-LDH

The nickel nitrate hexahydrate is used as a Ni source. However, the cobalt nitrate hexahydrate was used as Co source. First, the Ni and Co sources were mixed in a molar ratio of 3 : 2. Then, the mixture was dissolved in DI water. The pH was adjusted to 9–10. The resultant solution (**solution B**) was stirred for 60 min.

3.3. Synthesis of LDH-rGO-NS

Solution A and solution B were mixed followed by stirring for 1 h. Then it was shifted to Teflon lined autoclave. Then it was hydrothermally treated at 180 °C (12 h). The resultant product was separated by vacuum filtration. Then it was thoroughly washed with DI water and ethanol. Lastly, it was dried out under a vacuum at room temperature.

3.4. Materials characterization

High-resolution X-ray diffraction (HR-XRD) characterization was done using a diffractometer (Empyrean, PAN analytical, USA). The Raman spectra were obtained using a confocal

Raman spectrometer (Nicolet Almega XR Raman, Thermo Fisher Scientific, USA). The used excitation wavelength was 532 nm. X-ray photoelectron spectrometry (XPS: Thermo Scientific, ESCALAB 250Xi) was used to study the elemental composition of the LDH-rGO-NS. It was equipped with a monochromatic Al Kα X-ray source (1486.6 eV). The XPS was operated under an ultra-high-vacuum apparatus. XPS C 1s peak was used to calibrate concerning to other elements. Field emission scanning electron microscopy (FE-SEM) images were obtained using FE-SEM (Hitachi, S-4800). Transmission electron microscopy (TEM) and high-resolution TEM (HRTEM: HF-3300/NB5000/S-4800, Hitachi, Japan) were used to analyze the atomic structure of LDH-rGO-NS. Nitrogen adsorption–desorption analysis was conducted at 77 K using an analyzer (Micromeritics, Flex 3.02, USA).

3.5. Electrode formation and electrochemical characterization

Before the electrode formation, the nickel foams were cleaned in 10% HCl *via* sonication and rinsed in deionized (DI) water. Finally, foams were dried in an oven under a vacuum. The working electrode was made using slurry (containing 80 wt% LDH-rGO-NS, 10 wt% polyvinylidene fluoride (PVDF), and 10 wt% super P dissolved in ethanol) uniformly coated onto cleaned Ni-foam. It was dried at 120 °C (in a vacuum). Finally, a pressure of 10 MPa was applied for 60 s.

For the fabrication of asymmetric supercapacitors, the positive electrode was prepared by LDH-rGO-NS using the above procedure. However, activated carbon (AC) and cellulose acetate membrane was used as negative electrode and separator, respectively. 6.0 M KOH was used as an electrolyte. For the negative electrode formation, AC, super P, PVDF were used in the weight ratio of 8 : 1 : 1. The slurry was made in ethanol. The weight ratio of the positive and negative electrodes was determined using relation $m_+/m_- = (C_-\Delta V_-)/(C_+\Delta V_+)$. C_- and C_+ are the specific capacitance of the negative and positive electrodes, however, ΔV_- and ΔV_+ are the working potential of the negative and positive electrodes. The active mass used for the negative electrode was ∼8.5 mg.

The electrochemical properties were determined using a three-electrode system. A potentiostat (VersaSTAT3, Princeton Applied Research, USA) was used for measurement. LDH-rGO-NS (in the nickel foam, the loading mass of LDH-rGO-NS is ∼1 mg cm^{-2}) is used as a working electrode.[6] However, Pt and Hg/HgO were used as the counter and reference electrodes, respectively. The electrodes were characterized using electrochemical impedance spectroscopy (EIS), cyclic voltammetry (CV), and galvanostatic charge–discharge (GCD) in a 6 M KOH aqueous solution. The EIS measurement was done in a frequency range of 0.05 Hz to 100 kHz by applying AC voltage with 5 mV perturbation. The EIS data were analyzed using Nyquist plots, presenting the real (Z') and imaginary (Z'') parts of impedance. The CV curves were obtained at sweep rates (ν) of 2, 5, 20, 50, 100, and 200 mV s^{-1} in the voltage-sweep mode with the potential window from 0.1 to 0.6 V (*vs.* Hg/HgO). The GCD

measurement was conducted in the potential range of 0–0.5 V (*vs.* Hg/HgO) at the current densities of 5, 10, 20, and 50 A g^{-1}.

4. Results and discussion

4.1. Structural and morphological properties

The Ni–Co-LDHs are wrapped with N and S co-doped rGO-NS *via* a single-step synthesis process. The schematic of LDH-rGO-NS is illustrated in Fig. 1. To study the structural phase of GO, RGO-NS, Ni–Co-LDH, and LDH-rGO-NS, XRD characterization was done in the 2θ range from 5° to 60° as shown in Fig. 2a. The diffraction peak of GO appears at $2\theta = 10.37°$ corresponding to (002) plane.[18] This peak was abruptly shifted to $2\theta = 22.15°$ after reaction with thiourea and hydrothermal process which indicates a reduction in the value of interlayer spacing (*d*-spacing).[18] The *d*-spacing (d_{002}) between parallel basal planes of GO and rGO-NS were calculated corresponding to (002) planes. The obtained d_{002} value of GO (8.5 Å) was quite larger than the *d*-spacing of pristine graphite ($d_{002} = 3.37$ Å corresponding to $2\theta = 26.4°$). Thus, it confirms the proper oxidation of graphite flacks.[19] However, the *d*-spacing of rGO-NS was further reduced to 4.0 Å. The *d*-spacing value is compressed owing to the elimination of oxygen-related functional groups. Thus, a significant reduction of GO arisen thru the hydrothermal process. Moreover, one additional peak at $2\theta = 42.66°$ was observed which is ascribed to the (101) plan.[18] The broad diffraction peak of rGO-NS indicates that the *d*-spacing of graphite was expanded by the exfoliation. The XRD plot of Ni–Co-LDH shows the diffraction peaks at $2\theta = 11.28°$, 22.57°, 34.46°, and 38.49° corresponding to the (003), (006), (009), and (015) planes, respectively. These XRD peaks were agreed with the hydrotalcite-like LDH.[20] The XRD plot of LDH-rGO-NS is analogous to pure Ni–Co-LDH, which validates the presence of Ni–Co-LDH in the LDH-rGO-NS.[21] Moreover, the influence of rGO-NS can be seen in the XRD spectrum of LDH-rGO-NS (red dotted circle), which confirms the existence of rGO-NS. A similar observation has been made by Lonkar *et al.*[21]

Further, the GO, rGO-NS, Ni–Co-LDH, and LDH-rGO-NS samples are characterized by Raman spectroscopy. These Raman spectra are displayed in Fig. 2b. In the GO sample, four Raman peaks are observed at 1354, 1594, 2677, and 2922 cm^{-1}
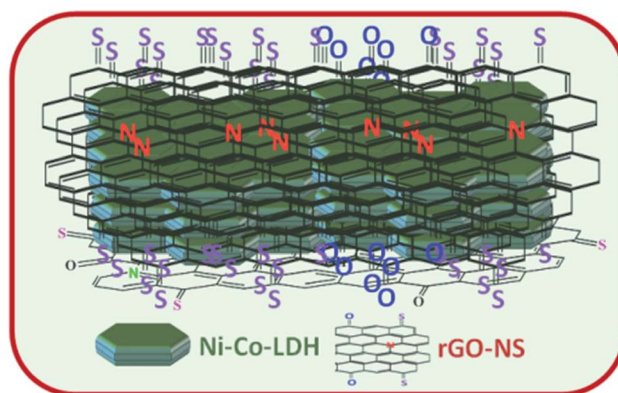

Fig. 1 Schematic of LDH-rGO-NS structures synthesized using N and S co-doped graphene, and N–Co-layered hydroxide.
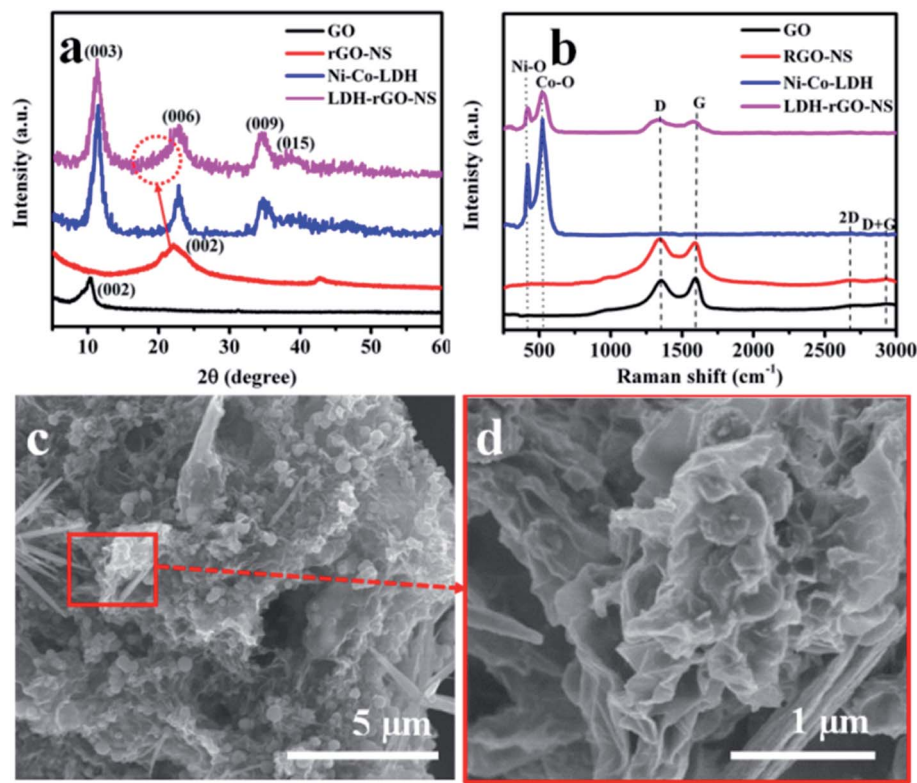
Fig. 2   (a) XRD, (b) Raman spectra of GO, RGO-NS, and LDH–rGO-NS, and (c and d) FE-SEM images of the LDH–rGO-NS.

designated as D, G, 2D, and D + G, respectively. The D and G peaks are related to the in-plane vibration of sp^2 carbon atoms and defects in the GO sample, respectively.[22] The D peak is downshifted to 1337 and 1332 cm^{-1} for rGO-NS and LDH–rGO-NS, respectively. The downshifting of the D peak may have occurred because of N doping and S doping.[23,24] The peak positions of G, 2D, and D + G were unaffected for rGO-NS. In the LDH–rGO-NS sample, the peaks corresponding to 2D and D + G bands were disappeared, while peaks associated with D and G bands are present with lower intensity. The Raman spectrum of Ni–Co-LDH shows two main peaks at 417 and 528 cm^{-1} designated to the vibrational mode of Ni–O, and Co–O, respectively.[20,25] Therefore, these two peaks also appeared in the sample in the LDH–rGO-NS sample. LDH–rGO-NS not only reveal the peaks of Ni–Co-LDH but also retain D and G bands of rGO-NS. This result revealed the presence of Ni–Co-LDH and rGO-NS in LDH–rGO-NS sample.

The obtained intensity ratio of the D and G peaks (I_D/I_G) for GO, rGO-NS, and LDH–rGO-NS are found to be 0.96, 1.13, and 1.11, corresponding to a reduction of GO and an increase in disorder of the graphene. The increase in the I_D/I_G value suggests the creation of compact sp^2 graphitic domains with the reduction of GO.[21,26]

The FE-SEM images of GO, rGO-NS, and Ni–Co-LDH are displayed in Fig. S1.† The nano-sheet-like structure is obtained for the Ni–Co-LDH. However, the FE-SEM images of the LDH–rGO-NS are displayed in Fig. 2(c and d). The Ni–Co-LDH structures are enfolded well by wrinkled rGO-NS (Fig. 2c). The rGO-NS are doped and reduced during the heating of the mixture

solution with the thiourea. The Ni–Co-LDH is positively charged, while the rGO-NS is negatively charged and the Ni–Co-LDH is consequently well wrapped with rGO-NS in the synthesized LDH–rGO-NS. Thus, during the stirring process of the mixture solution of RGO-NS and Ni–Co-LDH, the Ni–Co-LDHs are properly wrapped off with the rGO-NS because of electrostatic interaction between them (Fig. 2d). Thus, RGO-NS wrapped Ni–Co-LDH offers decent flexibility to bear the volume expansion of the Ni–Co-LDH throughout the charge–discharge cycling. The doping of elements and elemental dispersal in Ni–Co-LDH is inspected by the EDS mapping was conducted as shown in Fig. 3(a–f). The present elements are C, Ni, Co, O, S, and N. These elements are homogeneously distributed. Moreover, the TEM image of LDH–rGO-NS confirms a proper wrapping of Ni–Co-LDH with the graphene (Fig. 4a). The rGO-NS have 4–5 layers, which wrap well the Ni–Co-LDH. Furthermore, the HRTEM characterization was used to study the crystallinity of the LDH–rGO-NS. The lattice fringes with d-spacing of ca. 3.93, 2.60, and 2.34 Å are observed to correspond to the (006), (009), and (015) planes, respectively (Fig. 4b). These planes are also observed in the XRD pattern.[27] Furthermore, the specific surface area of the Ni–Co-LDH and LDH–rGO-NS is determined by the Brunauer–Emmett–Teller (BET) technique. The obtained BET surface areas are 95.4, 27.5, and 131 cm^2 g^{-1} for rGO-NS, Ni–Co-LDH, and LDH–rGO-NS, respectively (Fig. S2†). This result revealed that after insertion of rGO-NS, the BET surface area is enhanced greatly, which is advantageous for the electrode.
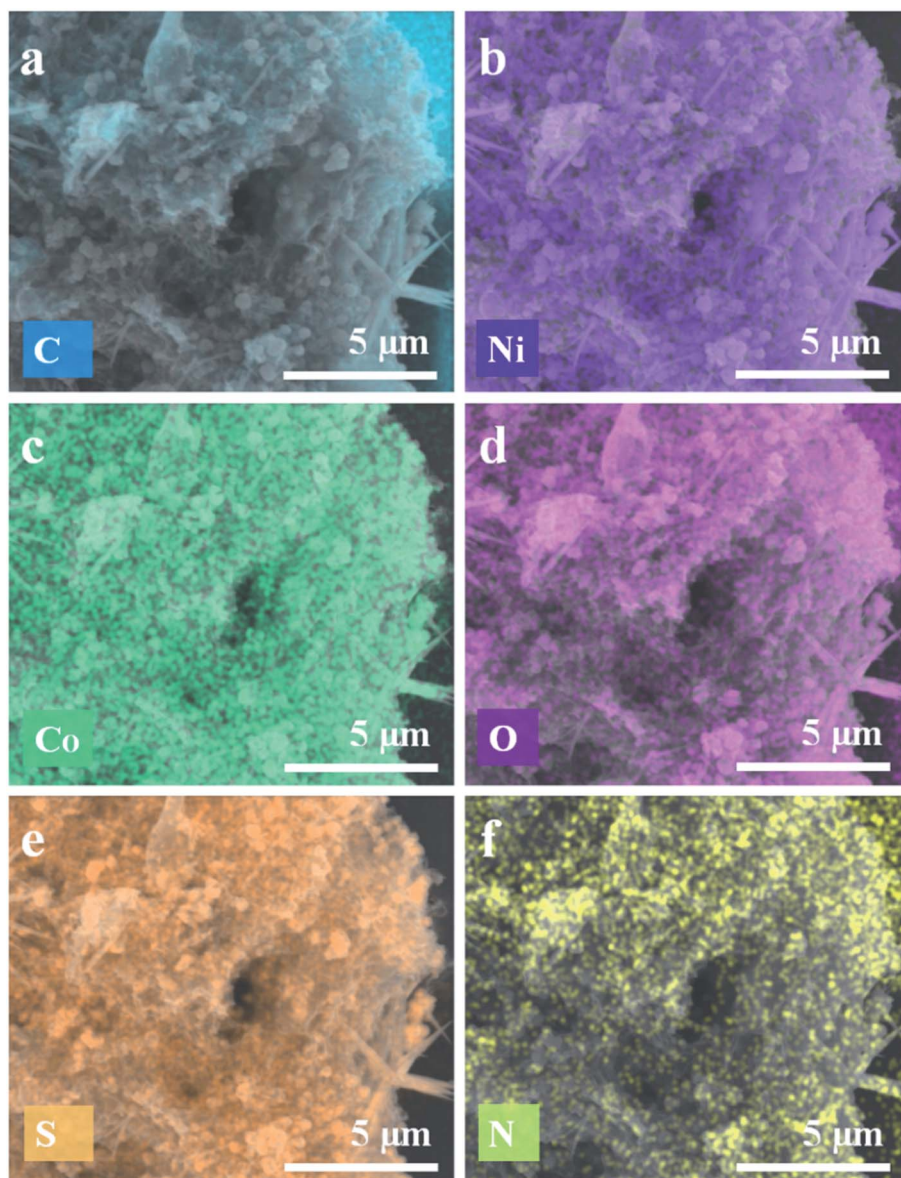
Fig. 3 EDS mapping of LDH-rGO-NS for (a) C, (b) Ni, (c) Co, (d) O, (e) S, and (f) N.
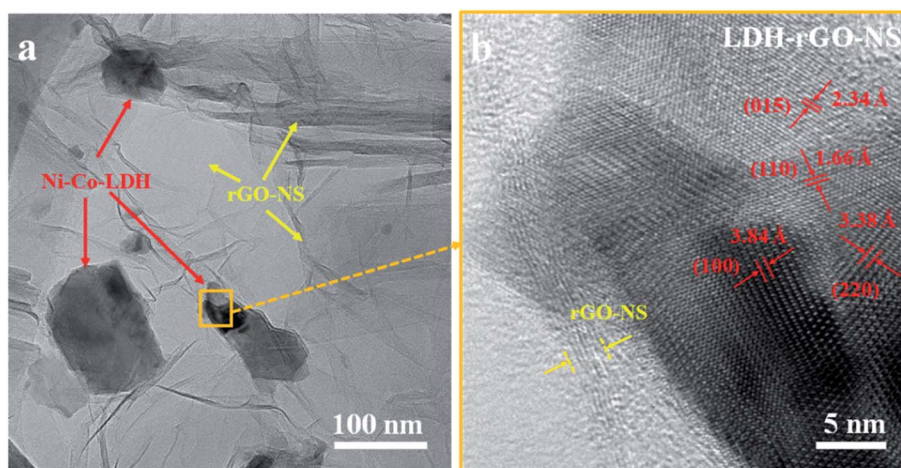

Fig. 4 (a) TEM, and (b) HRTEM images of LDH-rGO-NS.

4.2. Elemental analysis

The elemental composition was also analyzed using the XPS characterization technique. The XPS survey spectra are illustrated in Fig. S3.† It approves the existence of the C, Ni, Co, O, S, and N elements in the LDH-rGO-NS.[28] The XPS signature of C, Ni, Co, S, and N peaks obtained by the detailed scan are displayed in Fig. 5(a–e). The Gaussian–Lorentzian function is employed to fit XPS data. However, the Shirley technique is employed for background rectification.[29] The XPS C 1s spectra are deconvoluted into five main components as displayed in Fig. 5a. The deconvoluted peaks obtained at 282.42, 284.41, 285.60, 287.82, and 291.11 eV are ascribed to C-M (M = Ni or Co), C–C/C=C, C=N/C–O/C–S, C–N/C=O, and O–C=O, respectively.[24,30–32] The obtained corresponding percentage of C-bonding is 13.20%, 9.35%, 6.99%, 44.26%, and 26.20%. The

presence of C–N & C–S bonds confirm the N and S doping in the graphene. The existence of C–Ni & C–Co indicates dealing amongst Ni–Co-LDH and rGO-NS.

The XPS scan of the Ni 2p spectrum is displayed in Fig. 5b. There are two main peaks at 856.19 and 873.64 eV associated with Ni^{2+} characteristics of Ni $2p_{3/2}$ and Ni $2p_{1/2}$, respectively.[33] The space between these two peaks (ΔE) is ~17.45 eV, which is approximately the same as the standard spacing between Ni $2p_{3/2}$ and Ni $2p_{1/2}$ of Ni^{2+} state in NiO,[34] thus confirming the dominating valence state of Ni^{2+} in Ni–Co-LDH. Moreover, two additional peaks associated with shakeup satellites (denoted by Sat.) of Ni $2p_{3/2}$ and Ni $2p_{1/2}$ are obtained at 862.2 and 879.59 eV, respectively. However, four peaks are obtained for Co 2p associated with Co $2p_{3/2}$ and Co $2p_{1/2}$. The $2p_{3/2}$ peak is composed of two peaks corresponding to Co^{3+} and Co^{2+} located at 780.46 and
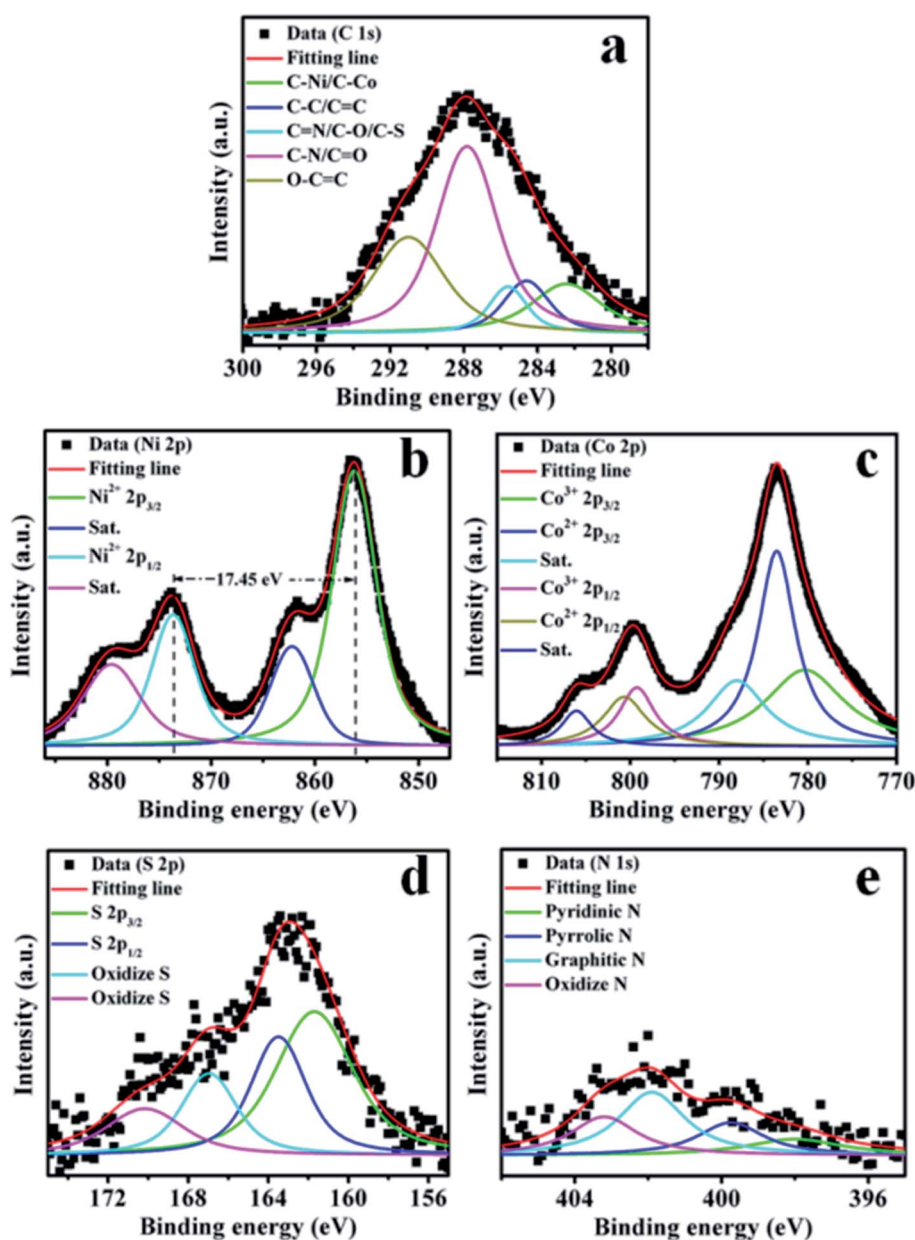

Fig. 5 XPS spectra of (a) C 1s, (b) Ni 2p, (c) Co 2p, (d) S 2p, and (e) N 1s scan for LDH–rGO-NS.

© 2021 The Author(s). Published by the Royal Society of Chemistry

783.41 eV, respectively. Similarly, the $2p_{1/2}$ peak is also deconvoluted into two peaks analogous to Co^{3+} and Co^{2+} situated at 799.23 and 800.89 eV, respectively (Fig. 5c).[35] Moreover, two additional peaks associated with shakeup satellites of Co $2p_{3/2}$ and Co $2p_{1/2}$ are obtained at 785.62 and 803.15 eV, respectively. A low-intensity peak corresponding to Co $2p_{3/2}$ is demonstrating the existence of both Co^{3+} and Co^{2+} in LDH-rGO-NS.[8,36,37] However, the spacing between Co $2p_{3/2}$ and Co $2p_{1/2}$ is 16.42 eV indicating that the dominant valence state is Co^{2+}, which is slightly larger than the earlier stated values of 15.90 eV (ref. 15) and 15.70 eV.[7]

The deconvoluted XPS S 2p spectra are displayed in Fig. 5d. Two peaks are corresponding to S $2p_{3/2}$ and S $2p_{1/2}$ located at 161.71 and 163.49 eV, respectively. The spacing between these two peaks is 1.78 eV, which is quite larger than the pristine S.[34] Moreover, two peaks associated with oxidized S of lower intensity are observed at 166.9 and 170.2 eV.

Fig. 5e shows a detailed XPS N 1s peak. The N 1s spectrum is deconvoluted into four peaks positioned at 398.01, 399.72, 401.89, and 403.21 eV, which correspond to pyridinic-N, pyrrolic-N, graphitic-N, and oxidized-N, respectively.[16,18] The obtained corresponding percentage of N moieties is 14.48%, 20.79%, 40.25%, and 24.48%, respectively. It can be seen that graphitic N has a maximum fraction, which can act as a strong electron-donating group to the aromatic π-system.[18,38]

4.3. Electrochemical properties

The electrochemical performance of the electrode materials is assessed using EIS, CV, and GCD. Fig. 6a shows the CV curves of LDG-rGO-NS at ν value of 2, 5, 20, and 50 mV s^{-1}. Besides, Fig. S4† displayed the CV curves for higher san rates (100 and 200 mV s^{-1}). The CV curves at various ν values offer a couple of strong redox peaks because of the pseudo-capacitive behavior of $M(OH)_2$/MOOH.[39] These peaks are arising owing to the alteration of Ni^{2+}/Ni^{3+} and Co^{2+}/Co^{3+} ions adsorbed onto the exterior of Ni–Co-LDH throughout the redox reaction.[16] The expected reactions involved to arise the redox peaks would be given by eqn (1) and (2)[40,41]

$$Ni(OH)_2 + OH^- \rightarrow NiOOH + H_2O + e^- \quad (1)$$

$$Co(OH)_2 + OH^- \rightarrow CoOOH + H_2O + e^- \quad (2)$$

The effectiveness of the above charge storing mechanisms is evaluated by determining the b-value of the relation (3)[42]

$$i_p = a\nu^b \quad (3)$$

where i_p is the anodic or cathodic current, a is an adjustable parameter,[43] and b-value delivers the perception concerning the charge storing mechanism.[44,45] The b-value of the cathodic and anodic reactions are calculated using the slope of the curve $\log(i_p)$ *vs.* $\log(\nu)$ as illustrated in Fig. 6b. The obtained slopes for the anodic and cathodic b-values are 0.73 and 0.72, respectively. The slope of the LDH-rGO-NS is greater than the previously reported values,[15,24] revealing a faster ion (charge) transportation rate in the LDH-rGO-NS. The enhancement of the charge transportation rate is due to the wrapping of Ni–Co-LDH
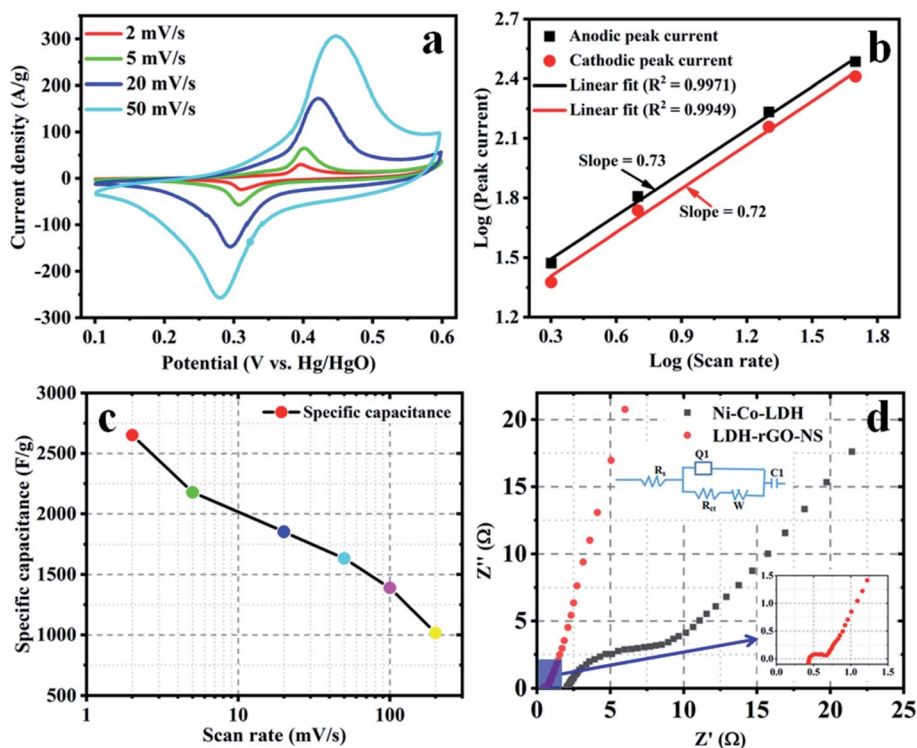

Fig. 6 Electrochemical characterization (a) cyclic-voltammetry at various sweep rates, (b) log(peak current) *vs.* log(sweep rate), (c) specific capacity as a function of sweep rate, and (d) EIS of LDH-rGO-NS electrode.

with rGO-NS. The combined impact of conductivity and heteroatoms (N and S) caused a great improvement in the charge transportation rate.

It can be noted that the spacing between anodic and cathodic peaks increases with the rise in v value. However, the appearance of the curves is unchanged. The specific capacitances (C_s) at various v is determined by the relation (4)[8]

$$C_s = \frac{\int_{V_1}^{V_2} I \, dt}{2vm(V_2 - V_1)} \quad (4)$$

where $\int_{V_1}^{V_2} I \, dt$ is the charge, which is determined by integration of the CV curve, m = active mass of the electrode (g), and ($V_2 - V_1$) = potential window (V).

The obtained values of C_s are 2651, 2178, 1853, 1633, 1388, and 1016 F g^{-1} at v = 2, 5, 20, 50, 100, and 200 mV s^{-1}, respectively. The C_s value at a v = 20 mV s^{-1} is ~70% of the C_s value obtained at 2 mV s^{-1} (Fig. 6c). However, the capacity of Ni–Co-LDH is obtained as 1226 F g^{-1}, which is quite lower than the LDH-rGO-NS (Fig. S5†). The stability of the electrode materials was tested using a long-cycled CV measurement. The CV of 1st, 1000th and 2000th cycles at a v = 100 mV s^{-1} are shown in Fig. S6.† The obtained results revealed that the retention rate is ~71% at the v = 100 mV s^{-1} after 2000 cycles.

The ion/charge transportation was investigated using EIS measurement. The Nyquist plots of the Ni–Co-LDH and LDH-rGO-NS electrodes are displayed in Fig. 6d (inset shows the equivalent circuit), which revealed the value of series resistance (R_s) and charge transfer resistance (R_{ct}). Usually, the Nyquist plot consists of two different fragments: a semicircle is obtained in the mid-high frequency section, while a lined shape is formed in the low-frequency region. The EIS data is used to fit using an equivalent circuit (inset of Fig. 6d).[37] The initial point of the semicircle gives the value of R_s, whereas the diameter provides the value of R_{ct}. R_s is indicative of the resistivity of the electrode materials, R_{ct} is associated with faradaic reactions and double-layer capacitance.[46] The constant phase element (Q1) is responsible for the double-layer capacitance. However, W and $C1$ are the Warburg resistance and limiting capacitance. W is due to ion diffusion and transportation in the electrolyte. The obtained values of R_s and R_{ct} for the LDH-rGO-NS electrode are found to be 0.43 and 0.24 Ω, respectively. However, the obtained

R_s and R_{ct} values are 2.15 and 7.83 Ω, respectively. The R_s value of LDH-rGO-NS is slightly higher than the Ni–Co-LDH composite with N-doped rGO (LDH-rGO-N) (0.31 Ω) obtained by Wang et al.[16] but quite lower than the composite Ni–Co-LDH and rGO (Ni–Co-LDH/rGO) (1.099 Ω) obtained by Le et al.[15] This confirms that the LDH-rGO-NS offers good conductivity (inset of Fig. 6d). Moreover, the obtained value of R_{ct} of LDH-rGO-NS is 0.24 Ω, which is similar to LDH/rGO (0.22 Ω) showed by Le et al.[15]

GCD characterization is used for an additional assessment of the electrochemical performance of the LDH-rGO-NS electrode. Fig. 7a shows the discharge characteristics of the LDH-rGO-NS electrode at various current densities of 5, 10, 20, and 50 A g^{-1}. However, the discharge characteristics of the LDH-rGO electrode are shown in Fig. S7† for comparison. The discharge curves were used to determine the specific discharge capacitance (C_{ds}) at various discharge current (I) using relation (5)[15]

$$C_{ds} = \frac{I\Delta t}{m(\Delta V)} \quad (5)$$

where, Δt = discharge time (s) and ΔV = potential drop.

The obtained C_{ds} values of LDH-rGO-NS electrode are 2193, 1806, 1556, and 1290 F g^{-1} at the discharge current density of 5, 10, 20, and 50 A g^{-1}, respectively. However, the C_{ds} values of LDH-rGO obtained at 5, 10, 20, and 50 A g^{-1} are 2050, 1646, 1352, and 1060 F g^{-1}, respectively. The dependency of the C_{ds} on discharge current density can be seen in Fig. 7b. The values of C_{ds} of LDH-rGO-NS is quite higher than the values LDH-rGO electrode. Furthermore, the obtained discharge capacitance of values of the LDH-rGO-NS electrode is compared in Table 1. The C_{ds} value of LDH-rGO-NS is larger than the values achieved in earlier reports associated with LDH/rGO-based materials.[15,37,47–51] In LDH-rGO-NS, the electrochemical performance is enhanced due to an excellent ion/charge transfer rate because of N and S co-doping.

The energy density (E) and power density (P) are determined using eqn (6) and (7), respectively.[8]

$$E = \frac{I}{3.6m'} \int V \, dt \quad (6)$$
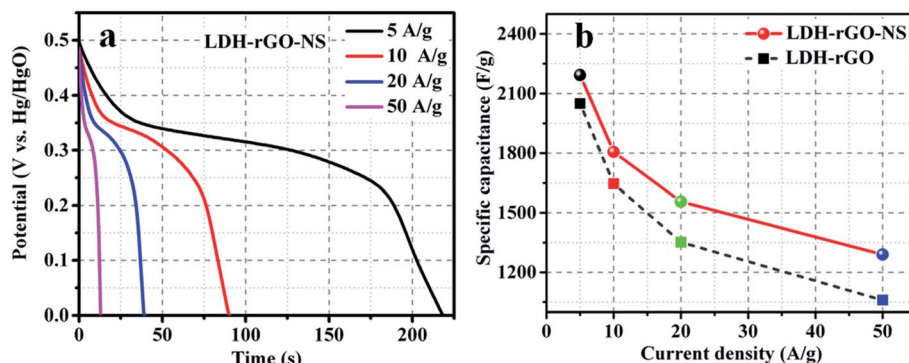
$$P = \frac{E}{\Delta t} \quad (7)$$

Fig. 7 Electrochemical characterization (a) galvanometric discharge curves at various discharge current densities (5, 10, 20, 50 A g^{-1}) and (b) specific capacity as a function of discharge current density of LDH-rGO-NS electrode.

Table 1 Comparison of the specific capacitance of various LDH-based materials

Electrode materials	Specific discharge capacitance (F g^{-1})	Discharge current density (A g^{-1})	Electrolyte (KOH) concentration	Loading mass (mg cm^{-2})	Ref.
Ni–Co-LDH/rGO	2004, 2130	5.0, 2.0	3 M	2.1	15
Ni–Co-LDH/rGO-N[a]	1720	3.0	6 M	1.0	16
Ni–Co-LDH/graphene sheet	1980.7	1.0	6 M	—	48
Ni–Co-LDH/rGO	1911	2.0	3 M	1.5	37
Ni–Co-LDH/rGO	1691	0.5	6 M	3.0	49
Ni–Al-LDH/act-rGO[b]	1173	1.0	6 M	—	50
Co–Al-LDH/rGO	1962	1.0	6 M	—	51
LDH-rGO-NS	2193	5.0	6 M	1.0	This work

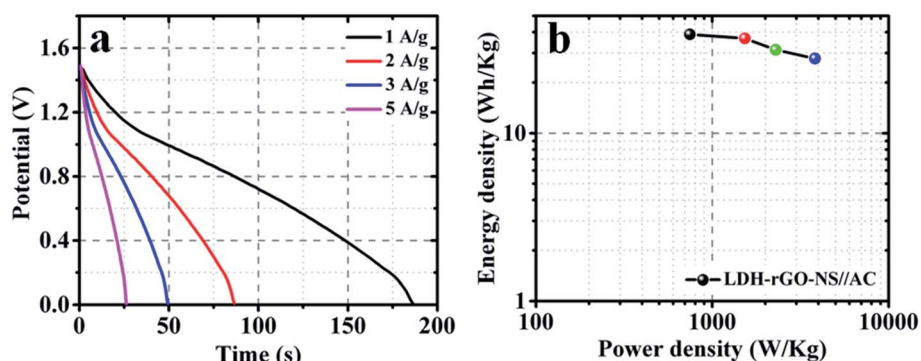[a] rGO-N = N-doped rGO. [b] Act-rGO = activated rGO.

Fig. 8 Electrochemical characterization (a) galvanometric discharge curves at various discharge current densities and (b) Ragone plot of the LDH-rGO-NS//AC asymmetric supercapacitors.

where, m' is the sum of the active masses of LDH-rGO-NS and AC.

GCD curves of the LDH-rGO-NS//AC supercapacitors at various are illustrated in Fig. 8a. The discharge curves were used to determine the values of E and P. The obtained energy density and power density are shown in the Ragone plot (Fig. 8b). The obtained energy density is 38.8 W h kg^{-1} at a power density of 746.5 W kg^{-1}. Even at a power density of 3827.9 W kg^{-1}, the obtained energy density is 27.8 W h kg^{-1}.

5.   Conclusions

The single-step hydrothermal process was used to synthesize LDG-rGO-NS. Various techniques were used to characterize the LDH-rGO-NS sample. The XRD and Raman studies of LDH-rGO-NS revealed the presence of both Ni–Co-LDH and graphene. The FE-SEM results confirmed that the shape of the Ni–Co-LDH was spherical. The Ni–Co-LDH structures are swathed well by wrinkled rGO-NS. The XPS C 1s spectra established the existence of N and S doping in the rGO. The superior values of the anodic (0.73) and cathodic (0.72) b-value were accomplished. Moreover, the EIS result showed that the LDH-rGO-NS electrode proposes a good charge transfer resistance of 0.24 Ω. The electrochemical performance was enhanced due to an excellent ion/charge conductance because of N and S co-doping. The existence of C–Ni & C–Co peaks confirmed that an interaction occurs between Ni–Co-LDH and rGO-NS. The obtained specific

capacities were 2651, 2178, 1853, 1633, 1388, and 1016 F g^{-1} at ν = 2, 5, 20, 50, 100, and 200 mV s^{-1}, respectively. The retention rate obtained after 2000 cycles was ~71% at ν = 100 mV s^{-1}. Besides, the specific capacity values obtained from GCD are 2193, 1806, 1556, and 1290 F g^{-1} at the discharge current density of 5, 10, 20, and 50 A g^{-1}, respectively. The achieved energy density of the LDH-rGO-NS//AC asymmetric supercapacitors was 38.8 W h kg^{-1} at the power density of 746.5 W kg^{-1}. The LDH-rGO-NS can be a potential candidate as an electrode material for high-performance electrochemical energy storage devices.

Ethical statement

This article does not contain any studies with human or animal subjects.

Conflicts of interest

The author declares no conflict of interest.

Acknowledgements

References

1 F. Wang, Z. Zuo, L. Li, F. He, F. Lu and Y. Li, *Adv. Mater.*, 2019, **31**, 1806272.

2 L. Li, Z. Zuo, F. Wang, J. Gao, A. Cao, F. He and Y. Li, *Adv. Mater.*, 2020, **32**, 2000140.

3 M. Yu, Z. Wang, Y. Han, Y. Tong, X. Lu and S. Yang, *J. Mater. Chem. A*, 2016, **4**, 4634–4658.

4 A. Muzaffar, M. B. Ahamed, K. Deshmukh and J. Thirumalai, *Renewable Sustainable Energy Rev.*, 2019, **101**, 123–145.

5 T. Li, R. Li and H. Luo, *J. Mater. Chem. A*, 2016, **4**, 18922–18930.

6 J. Wu, W.-W. Liu, Y.-X. Wu, T.-C. Wei, D. Geng, J. Mei, H. Liu, W.-M. Lau and L.-M. Liu, *Electrochim. Acta*, 2016, **203**, 21–29.

7 L. Sun, L. Wang, C. Tian, T. Tan, Y. Xie, K. Shi, M. Li and H. Fu, *RSC Adv.*, 2012, **2**, 4498.

8 B. Zhao, D. Chen, X. Xiong, B. Song, R. Hu, Q. Zhang, B. H. Rainwater, G. H. Waller, D. Zhen, Y. Ding, Y. Chen, C. Qu, D. Dang, C.-P. Wong and M. Liu, *Energy Storage Mater.*, 2017, **7**, 32–39.

9 J. H. Lee, S. H. Kwon, S. Kwon, M. Cho, K. H. Kim, T. H. Han and S. G. Lee, *Nanomaterials*, 2019, **9**, 268.

10 X. Li, D. Du, Y. Zhang, W. Xing, Q. Xue and Z. Yan, *J. Mater. Chem. A*, 2017, **5**, 15460–15485.

11 X. Sun, G. Wang, H. Sun, F. Lu, M. Yu and J. Lian, *J. Power Sources*, 2013, **238**, 150–156.

12 J. Yang, C. Yu, X. Fan and J. Qiu, *Adv. Energy Mater.*, 2014, **4**, 1400761.

13 T. Wang, L. X. Wang, D. L. Wu, W. Xia and D. Z. Jia, *Sci. Rep.*, 2015, **5**, 9591.

14 Z. S. Wu, A. Winter, L. Chen, Y. Sun, A. Turchanin, X. Feng and K. Mullen, *Adv. Mater.*, 2012, **24**, 5130–5135.

15 K. Le, Z. Wang, F. Wang, Q. Wang, Q. Shao, V. Murugadoss, S. Wu, W. Liu, J. Liu, Q. Gao and Z. Guo, *Dalton Trans.*, 2019, **48**, 5193–5202.

16 W. Wang, N. Zhang, Z. Ye, Z. Hong and M. Zhi, *Inorg. Chem. Front.*, 2019, **6**, 407–416.

17 J. P. Paraknowitsch and A. Thomas, *Energy Environ. Sci.*, 2013, **6**, 2839.

18 F. Khan, S.-H. Baek and J. H. Kim, *Carbon*, 2016, **100**, 608–616.

19 F. Khan and J. H. Kim, *J. Ind. Eng. Chem.*, 2018, **68**, 129–139.

20 H. Xu, J. Wu, J. Liu, Y. Chen and X. Fan, *J. Mater. Sci.: Mater. Electron.*, 2018, **29**, 17234–17244.

21 S. P. Lonkar, J. M. Raquez and P. Dubois, *Nano-Micro Lett.*, 2015, **7**, 332–340.

22 A. Kaniyoor and S. Ramaprabhu, *AIP Adv.*, 2012, **2**, 032183.

23 R. Lv, Q. Li, A. R. Botello-Mendez, T. Hayashi, B. Wang, A. Berkdemir, Q. Hao, A. L. Elias, R. Cruz-Silva, H. R. Gutierrez, Y. A. Kim, H. Muramatsu, J. Zhu, M. Endo, H. Terrones, J. C. Charlier, M. Pan and M. Terrones, *Sci. Rep.*, 2012, **2**, 586.

24 A. Das, S. Pisana, B. Chakraborty, S. Piscanec, S. K. Saha, U. V. Waghmare, K. S. Novoselov, H. R. Krishnamurthy, A. K. Geim, A. C. Ferrari and A. K. Sood, *Nat. Nanotechnol.*, 2008, **3**, 210–215.

25 J. Memon, J. Sun, D. Meng, W. Ouyang, M. A. Memon, Y. Huang, S. Yan and J. Geng, *J. Mater. Chem. A*, 2014, **2**, 5060.

26 R. Xie, G. Fan, Q. Ma, L. Yang and F. Li, *J. Mater. Chem. A*, 2014, **2**, 7880.

27 L. Shi, Y. Chen, R. He, X. Chen and H. Song, *Phys. Chem. Chem. Phys.*, 2018, **20**, 16437–16443.

28 L. Jiang, R. Zou, W. Li, J. Sun, X. Hu, Y. Xue, G. He and J. Hu, *J. Mater. Chem. A*, 2013, **1**, 478–481.

29 D. A. Shirley, *Phys. Rev. B*, 1972, **5**, 4709.

30 J. Zhou, J. Li, K. Liu, L. Lan, H. Song and X. Chen, *J. Mater. Chem. A*, 2014, **2**, 20706–20713.

31 S. Bian, C. Shen, Y. Qian, J. Liu, F. Xi and X. Dong, *Sens. Actuators, B*, 2017, **242**, 231–237.

32 F. Khan, M. Oh and J. H. Kim, *Chem. Eng. J.*, 2019, **369**, 1024–1033.

33 J. Zhao, J. Chen, S. Xu, M. Shao, Q. Zhang, F. Wei, J. Ma, M. Wei, D. G. Evans and X. Duan, *Adv. Funct. Mater.*, 2014, **24**, 2938–2946.

34 J. Moulder, W. Stickle, P. Sobol and K. Bomben, *There is no corresponding record for this reference*, Google Scholar, 1992, pp. 52–53.

35 C. Shang, S. Dong, S. Wang, D. Xiao, P. Han, X. Wang, L. Gu and G. Cui, *ACS Nano*, 2013, **7**, 5430–5436.

36 H. Chen, L. Hu, M. Chen, Y. Yan and L. Wu, *Adv. Funct. Mater.*, 2014, **24**, 934–942.

37 X. Cai, X. Shen, L. Ma, Z. Ji, C. Xu and A. Yuan, *Chem. Eng. J.*, 2015, **268**, 251–259.

38 S. Jalili and R. Vaziri, *Mol. Phys.*, 2011, **109**, 687–694.

39 T. Wang, S. Zhang, X. Yan, M. Lyu, L. Wang, J. Bell and H. Wang, *ACS Appl. Mater. Interfaces*, 2017, **9**, 15510–15524.

40 X. Wang, C. Yan, A. Sumboja, J. Yan and P. S. Lee, *Adv. Energy Mater.*, 2014, **4**, 1301240.

41 J. Li, M. Yang, J. Wei and Z. Zhou, *Nanoscale*, 2012, **4**, 4498–4503.

42 Y. Gogotsi and R. M. Penner, *ACS Nano*, 2018, **12**, 2081–2083.

43 C. Hou, Z. Tai, L. Zhao, Y. Zhai, Y. Hou, Y. Fan, F. Dang, J. Wang and H. Liu, *J. Mater. Chem. A*, 2018, **6**, 9723–9736.

44 P. Simon, Y. Gogotsi and B. Dunn, *Science*, 2014, **343**, 1210–1211.

45 T. Brousse, D. Bélanger and J. W. Long, *J. Electrochem. Soc.*, 2015, **162**, A5185–A5189.

46 J. W. Lee, J. M. Ko and J.-D. Kim, *Electrochim. Acta*, 2012, **85**, 459–466.

47 Y. Cao, G. Li and X. Li, *Chem. Eng. J.*, 2016, **292**, 207–223.

48 T. Yan, R. Li and Z. Li, *Mater. Res. Bull.*, 2014, **51**, 97–104.

49 H. Ma, J. He, D. B. Xiong, J. Wu, Q. Li, V. Dravid and Y. Zhao, *ACS Appl. Mater. Interfaces*, 2016, **8**, 1992–2000.

50 N. Yulian, L. Ruiyi, L. Zaijun, F. Yinjun and L. Junkang, *Electrochim. Acta*, 2013, **94**, 360–366.

51 L. Zhang, K. N. Hui, K. S. Hui and H. Lee, *Electrochim. Acta*, 2015, **186**, 522–529.